JOURNAL OF WATER AND LAND DEVELOPMENT
e-ISSN 2083-4535
Polish Academy of Sciences (PAN) Institute of Technology and Life Sciences – National Research Institute (ITP – PIB)

JOURNAL OF WATER AND LAND DEVELOPMENT
DOI: 10.24425/jwld.2022.140383
2022, No. 52 (I–III): 133–144

Assessment of soil erosion using the GIS-based erosion potential method in the Kebir Rhumel Watershed, Northeast Algeria

Amer Zeghmar[1)], Nadir Marouf[1)], Elhadj Mokhtari[2)]

[1)] University of Larbi-Ben-M'hidi, Faculty of Sciences and Applied Sciences, Department of Hydraulic, Laboratory of Functional Ecology and Environment, Laboratory of Natural Resources and Management of Sensitive Environments, PO Box 358, 04000 Oum El Bouaghi, Algeria

[2)] University Mohamed Boudiaf M'sila, Faculty of Technology, Department of Hydraulic, Algeria

RECEIVED 08.01.2021 REVIEWED 20.08.2021 ACCEPTED 10.09.2021

Abstract: Soil erosion is an important factor that should be considered when planning renewable natural resource projects, effects of which can be measured by modelling techniques. Therefore, disintegration models determine soil loss intensity and support soil conservation practices. This study estimates soil loss rates by water erosion using the Erosion Potential Method (EPM) in the Kebir Rhumel Watershed located in Northeast Algeria. The area is north to south sub-humid to semi-arid, receives irregular rainfall, and has steep slopes and low vegetation cover which makes it very vulnerable to erosion. The main factors in the EPM (soil erodibility, soil protection, slope, temperature, and rainfall) were evaluated using the Geographical Information System (GIS) and data provided by remote sensing technologies. The erosion intensity coefficient Z was 0.60, which indicates medium erosion intensity. While the results showed the average annual soil erosion of 17.92 $\mathrm{Mg \cdot ha^{-1} \cdot y^{-1}}$, maximum and minimum losses are 190.50 $\mathrm{Mg \cdot ha^{-1} \cdot y^{-1}}$ and 0.21 $\mathrm{Mg \cdot ha^{-1} \cdot y^{-1}}$, respectively. The EPM model shows satisfactory results compared to some studies done in the basin, where the obtained results can be used for more appropriate management of land and water resources, sustainable planning, and environmental protection.

Keywords: Erosion Potential Method, Geographic Information System (GIS), Kebir Rhumel, remote sensing, soil erosion, water erosion

INTRODUCTION

Soil erosion is one of the most prevalent forms of land degradation all over the world that causes many big environmental and socio-economic problems [IGHODARO *et al.* 2013]. It has several impacts, such as land degradation, reduced water quality, loss of the available storage capacity in water management structures, river sedimentation, road damage, and reduced agricultural productivity affecting sustainable development [PANAGOS *et al.* 2018; SHARDA *et al.* 2013; ZAKERINEJAD, MAERKER 2015]. Soil erosion by water is the process that separates particles in soil due to precipitation or runoff and then transports them with flowing water. It is followed by sedimentation in steep areas, reservoirs, irrigation systems and waterways [CERDÀ, DOERR 2008; EFTHIMIOU *et al.* 2016; KUNTA 2009]. Soil erosion is mainly caused by rain splash impact (separation), while rill and gully erosion are caused by flowing water (separation, transport) [CHAAOUAN *et al.* 2013; EFTHIMIOU *et al.* 2017; HAAN *et al.* 1994].

In the North of Algeria, soil erosion by water may lead to land degradation affecting several natural factors, such as climate, terrain, vegetation cover and soil quality. These are followed by human factors, such as expansion of agricultural land, deforestation, overgrazing, and urbanisation, overexploitation of fire wood, poor management, and improper conservation practices. All these factors constitute a major constraint to the development of agriculture and water resources management, and they increase the severity of soil erosion in the area [ABU HAMMAD 2011; MAZOUR, ROOSE 2002; MEDDI, TOUMI 2015; SAHLI *et al.* 2019]. According to the Ministry of Agriculture and Rural Development, 50 mln ha of land are threatened by water erosion. This represents more than 20% of the total area of the country, which is around 238 mln ha. Threatened areas are distributed over 14 mln ha of mountainous space in the north (affected by water erosion). As much as 80% of cultivated land exists in the most sensitive areas [Bouguerra *et al.* 2017; Bouhadeb *et al.* 2018; Mazour, Roose 2002; Meghraoui *et al.* 2017; Mostephaoui *et al.* 2013].

Many scientists and researchers seek to provide soil erosion models that are compatible with field data and those provided by remote sensing techniques by using geographic information systems (GIS) [Fernandez *et al.* 2003; Gitas *et al.* 2009; Nearing *et al.* 2005; Tang *et al.* 2015]. Several soil erosion models exist which can analyse, predict soil erosion, and identify vulnerable soil erosion areas. Among them is the Erosion Potential Method (EPM) developed by Gavrilović in watersheds of the Morava River in Serbia in 1962 [Efthimiou *et al.* 2017]. It seems to be one of major soil erosion models suitable for a large watershed and mountainous terrain [Globevnik *et al.* 2003].

The Erosion Potential Method (EPM) is an empirical semi-quantitative method that can estimate the average annual volume of soil detached by water and sedimentation volume, as well as determine spatial distribution of soil erosion intensity [Dragičević *et al.* 2017]. The EPM combines water erosion factors based on precipitation, temperature, soil erodibility, soil protection, types of erosion, and slopes [Sakuno *et al.* 2020; Solaimani *et al.* 2009]. The utilisation of the Gavrilović model requires mapping and combination of different parameters that are essential for the integration of the EPM model and the Geographic Information System (GIS) [Zahnoun *et al.* 2019]. The EPM model has been applied in many countries and has provided reliable results to qualify the severity of soil erosion, estimate average annual soil loss by water and sedimentation quantity, was well as to implement runoff regulation and erosion control measures [Efthimiou *et al.* 2016].

The objective of the present study is to provide mapping of soil erosion for the Kebir Rhumel Watershed by applying the EPM. The study uses the Geographic Information System (GIS) and data provided by remote sensing technologies. These are used to map the most important factors that affect soil particle separation and support quantitative and spatial estimation of soil loss rates due to water erosion. This helps to define measures that protect water resources and support land management.

STUDY AREA

The Kebir Rhumel Watershed is located in the North-East of Algeria (Fig. 1). It borders the Mediterranean Sea in the north, Constantine and Oum El Bouaghi in the east, Batna in the south, and Setif in the west. The site is situated between 5°40' and 6°40' E longitude and between 35°50' and 36°40' N latitude with a surface geographical area of 8843 km^2. It is considered to be one of the most important watersheds in the country, as it contains the largest dam in Algeria with the capacity of nearly $1 \cdot 10^9$ m^3.

The Kebir Rhumel Watershed is subdivided into two distinct parts, the western part, called by the Wadi Enndja basin, and the eastern part, called Wadi Rhumel. The Wadi Enndja Basin is located in the western part of the Kebir Rhumel Watershed. It has a surface area of 3454.85 km^2 and is characterised by a mountainous topography and relatively high precipitation (about 681.33 mm·y^{-1}). In this basin, the average elevation is 819.50 m, while the minimum and the maximum elevations are 114 and 1659 m. The Wadi Rhumel Basin extends from south to northeast. It is characterised by a softer topography and moderate precipitation (about 600 mm·y^{-1}). The surface area of this basin is 4062.42 km^2, the average elevation is 775.27 m, while the minimum and maximum elevations are 127 and 1722 m. Wadi El Kebir is the result of the confluence of two Wadis (Wadi Enndja and Wadi Rhumel) [Marouf, Remini 2011].

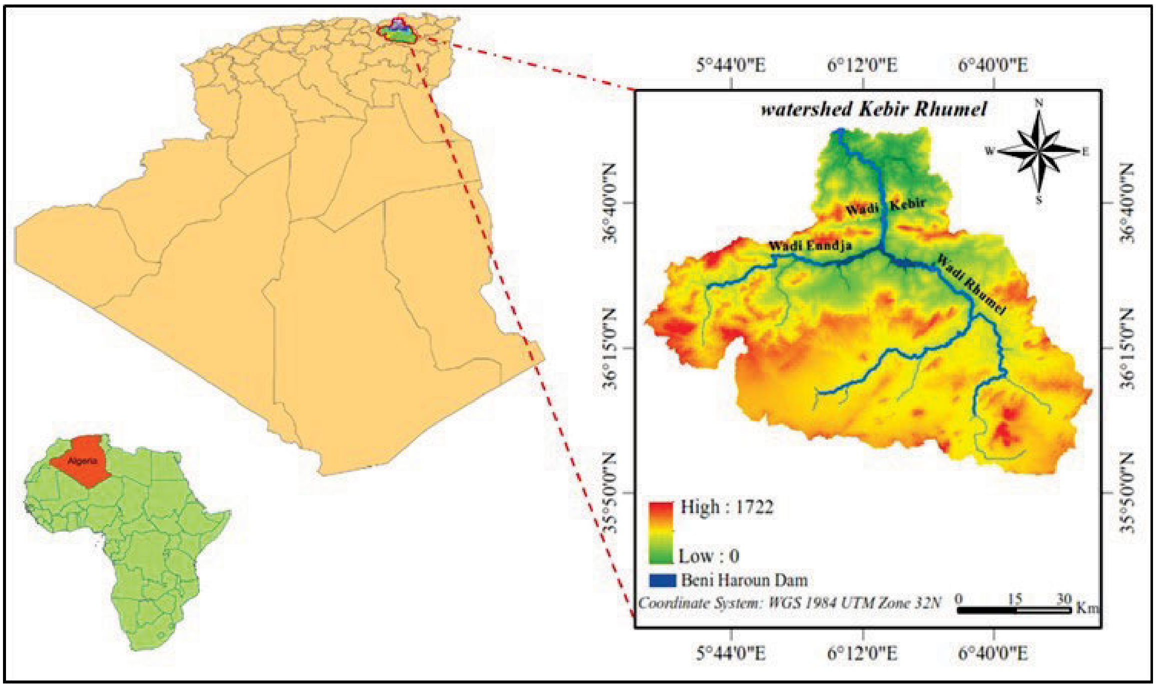

Fig. 1. Location of the Kebir Rhumel Watershed; source: own elaboration

The study area is characterised by a Mediterranean climate responsible for mild rainy winter and hot dry summer. Climate changes from semi-humid in the north to semi-arid in the south and diverse water resources are of different origins, i.e. rain, hail, and snow. In general, snow appears high up in the mountains. Thus, rainfall is the main factor that governs the flow of rivers and it has a direct effect on the flow. The annual average rainfall in the Kebir Rhumel Watershed is estimated between 638 and 738 mm. The rainfall is relatively abundant in the North, whereas it goes down dramatically as we move southward. The average annual temperature is 21.24°C, while the maximum and minimum temperatures are 31.3 and 12.15°C.

The Kebir Rhumel Watershed is characterised by a mountainous topography with steeper slopes concentrated mainly in its northern part. The average elevation is 745.12 m, while the minimum and maximum elevations are 0 and 1723 m (Fig. 1). The mean slope is 15.66%, where the very high slopes (exceeding 30%) occupy 14.55% of the total area concentrated mainly in the northwest part. The basin is characterised by an agricultural activity, e.g. wheat, barley, and fodder crops. The northern part is covered by oak and cork tree forests, while vegetation decreases in the southern part. This relatively low vegetation has affected the soil erosion phenomenon.

MATERIALS AND METHODOLOGY

MATERIALS

Erosion factors are estimated from data about soil, vegetation, climate, and topography available at websites. Data are shown in Table 1.

Table 1. Available datasets

Data	Resolution/ scale	Source	EPM factor
Precipitation data	–	National Agency for Hydraulic Resources (Fr. Agence Nationale des Ressources Hydrauliques – ANRH)	P_a
SRTM (DEM)	30 m	https://earthexplorer.usgs.gov/	J_a
ISRIC_WorldSoil Grids	250 m	https://soilgrids.org	Y
LANDSAT 8 OLI LANDSAT 5 TM	30 m	https://earthexplorer.usgs.gov/	X_a – T – φ

Explanations: P_a = average annual precipitation (mm·y^{-1}), J_a = slope index (%), Y = soil erodibility coefficient (–), X_a = soil protection coefficient against influences related to atmospheric phenomena, T = temperature coefficient (–), φ = existing erosion indicator (–).
Source: own elaboration.

METHODS

The EPM (Erosion Potential Method) estimates the average soil loss (m^3·km^{-2}·y^{-1}), and as a model it was developed by Gavrilović in watersheds of the Morava River, Serbia, in 1962 [Efthimiou *et al.* 2017]. The general methodology is based on six topical layers representing EPM factors, such as precipitation and temperature, soil erodibility, soil protection, existing erosion indicator and slopes, from climatic data, and remote sensing data. These are integrated into the EPM equation (Eq. 1) using a raster calculator available in ArcGIS 10.2:

$$W = TP_a\pi\sqrt{Z^3}F \tag{1}$$

where: W = average annual soil erosion (m^3·km^{-2}·y^{-1}), T = temperature coefficient, calculated by (Eq. 2).

$$T = \sqrt{\frac{T_0}{10} + 0.1} \tag{2}$$

T_0 = average annual temperature (°C), P_a = average annual precipitation (mm·y^{-1}), π = mathematical constant equal to 3.14159 (–), Z = erosion intensity coefficient (–), F = watershed surface area (km^2).
The erosion intensity coefficient (Z) is calculated by (Eq. 3).

$$Z = X_aY\left(\varphi + \sqrt{J_a}\right) \tag{3}$$

where: X_a = soil protection coefficient against influences related to atmospheric phenomena (–); Y = coefficient of soil erodibility (–); φ = existing erosion indicator that expresses the type of evolution of visible erosion processes in the watershed (–); J_a = slope index (%).

In order to estimate the total quantity (mass) of eroded sediments G (Mg·km^{-2}·y^{-1}) according to the steps outlined in the following organisation chart (Fig. 2), we use Equation (4):

$$G = W \cdot \rho \tag{4}$$

where: G = average annual soil erosion (Mg·km^{-2}·y^{-1}), W = average annual soil erosion (m^3·km^{-2}·y^{-1}), ρ = density (Mg·m^{-3}).

It is necessary to define the proportion of sediments that reach the reservoir in order to compare them directly with reservoir sediments. Most predictive water erosion models do not consider the delivery, deposition, or the transportation of sediments into water bodies. The EPM is innovative, since it introduces a new sediment delivery coefficient form, namely the retention coefficient *DR*, which estimates the amount of sediment retained along the basin (sediment delivery, deposition or routing within watercourse). The *DR* was calculated according to Zemljic [1971] using Equation (5):

$$DR = \frac{\sqrt{OD}\,(L + L_i)}{F(L + 10)} \tag{5}$$

where: F = watershed surface area (km^2), O = perimeter (km), L = major watercourse length (km), and L_i = secondary length; D = the average height distance of the catchment (km), it is calculated according to Globevnik *et al.* [2003] using Equation (6):

$$D = H_r - H_{\min} = (H_{\max} - H_{\min}) - H_{\min} \tag{6}$$

where: H_r (m) is the difference between the maximum ($H_{\max}$) and the minimum ($H_{\min}$) elevation. Specific Sediment Yield (*SSY*) is calculated by (Eq. 7):

$$SSY = DR \cdot W \tag{7}$$

This work was carried out according to steps outlined in the following chart (Fig. 2).

PARAMETERISATION OF EPM MODEL FACTORS

Temperature coefficient (*T*)

Heat is an essential indicator while forming mechanical weathering operations. It is important to determine its effect on fragmentation, fracture and breakage of rock grains, especially when daily thermal ranges increase, and role in the acceleration of these processes. It is particularly important in dry regions, as these have a clear impact on the moisture of rocks and sediments that lead to the decomposition, oxidation, and hydration of rock minerals [AbdulWahab, Jasim 2019].

Gavrilović sought to adopt temperature as an erosion factor in the EPM model. The values of the temperature coefficient are determined by a special formula (Eq. 2), which takes the annual average temperature as the basic variable to compute the coefficient (T). Satellite imagery was used to determine this indicator because there is absence of accurate climatic data related to temperature at meteorological stations in the Kebir Rhumel Watershed. The temperature was derived by converting the thermal range data from spectral radiation to the surface temperature using thermal constants in a MLT file using Landsat 5 Thematic Mapper (TM) and Landsat 8 (OLI/TIRS).

$$L_\lambda = \frac{L_{\max\lambda} - L_{\min\lambda}}{Q_{\mathrm{cal\,max}} - Q_{\mathrm{cal\,min}}}(Q_{\mathrm{cal}} - Q_{\mathrm{cal\,min}}) + L_{\min\lambda} \tag{8}$$

where: L_λ = spectral radiance (W·m^{-2}·sr^{-1}·μm^{-1}), Q_{cal} = quantised calibrated pixel value in Digital Number (DN), $L_{\min\lambda}$, $L_{\max\lambda}$ = spectral radiance (W·m^{-2}·sr^{-1}·μm^{-1}) scaled to $Q_{cal\ min}$ and $Q_{cal\ max}$, respectively, $Q_{cal\ min}$, $Q_{cal\ max}$ = the minimum and maximum of the quantised calibrated pixel value in DN, respectively.

Radiance values for Landsat 8 TIR can be retrieved from Equation (9) [Zanter 2018].

$$L_\lambda = M_L Q_{\mathrm{cal}} + A_L \tag{9}$$

where: M_L = band-specific multiplicative rescaling factor from metadata, Q_{cal} = quantised and calibrated standard product pixel value in Digital Number (DN), A_L = band-specific additive rescaling factor from metadata.

After radiance conversion, T_b from L_λ was computed by Equation (10).

$$T_b = \frac{K_2}{\ln\left(\frac{K_1}{L_\lambda} + 1\right)} \tag{10}$$

where: T_b = brightness temperature (K), K_1 (W·m^{-2}·sr^{-1}·μm^{-1}), K_2 (K) = calibration constants for Landsat TM, ETM+ and TIRS are shown in Table 2, L_λ = spectral radiance.

To convert Kelvins to Celsius degrees, we use Equation (11):

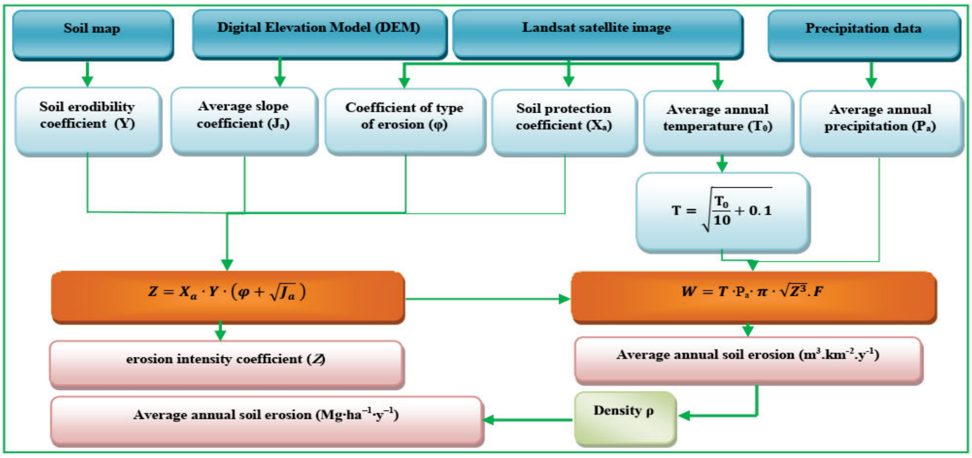

Fig. 2. Organisation chart of the methodology adopted; source: own elaboration

Landsat 5 TM presents six reflective bands (visible, near-infrared and short-wave infrared), with a native spatial resolution of 30 m and one band in thermal infrared (TIR) region (band 6). The spatial resolution for thermal infrared (band 6) is 120 m. The Landsat 8 OLI includes nine spectral bands that have a native spatial resolution of 30 m, except the panchromatic band (band 8) at a spatial resolution of 15 m, while Landsat 8 TIRS sensor covers two bands in the TIR region (band 10 and band 11), at a spatial resolution of 100 m [Sekertekin, Bonafoni 2020].

In this method, the TIR band was used for brightness temperature (T_b) estimation from Landsat imagery according to Plank's equation. There DN values for thermal band of Landsat 5 TM and 7 ETM+ can be directly converted into spectral radiance values using Equation (8) [Sekertekin, Bonafoni 2020]:

Table 2. Thermal band calibration constants for Landsat satellites

Satellite	K_1 (W·m^{-2}·sr^{-1}·μm^{-1})	K_2 (K)
Landsat 5 TM (band 6)	607.76	1 260.56
Landsat 7 ETM+ (band 6)	666.09	1 282.71
Landsat 8 TIRS (band 10)	774.89	1 321.08
Landsat 8 TIRS (band 11)	480.89	1 201.14

Explanations: K_1, K_2 = Landsat TM, ETM+ and TIRS thermal band calibration constants.
Source: own elaboration.

$$°C = Tb - 273.15 \quad (11)$$

The average annual temperature (°C) and the average annual temperature factor (T) (Fig. 3) were calculated using Landsat 5 and 8 satellite imagery for six years (1993; 1995; 2001; 2011; 2014; 2018).

The result shows spatial changes of the temperature coefficient, where we can notice an increasing gradient from the north to the south of the basin. The highest values (1.71) were registered in the southern basin which is characterised by scarcity of vegetation, while the lowest values (1.06) were found in the north of the basin with thick forests in mountainous areas.

agricultural work. Soil protection coefficient X_a levels are varied by land use from 0.05 (for dense forests) to 1 (for barren land) [Sakuno *et al.* 2020; Zahnoun *et al.* 2019]. The *NDVI* was calculated according to Equation (12) [Rousel *et al.* 1973; Sahli *et al.* 2019] based on Landsat satellite images:

$$NDVI = \frac{NIR - R}{NIR + R} \quad (12)$$

where: *NIR*, *R* = the spectral reflectances in the near-infrared and red band, respectively.

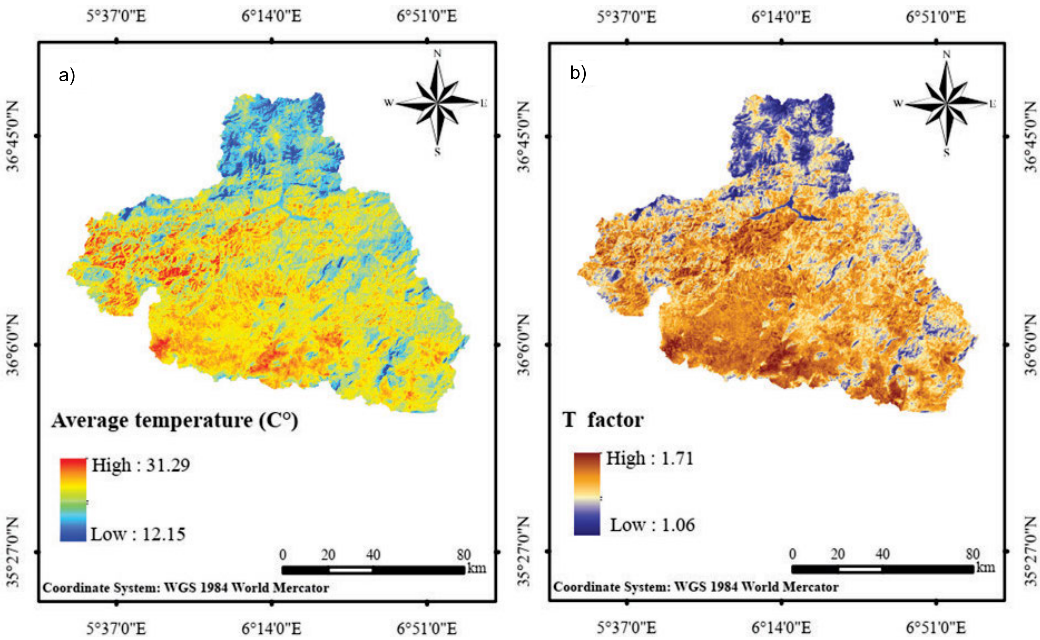

Fig. 3. Map of: a) annual average temperature (°C), b) annual average temperature coefficient T; source: own elaboration

Average annual precipitation (P_a)

Rainfall is a significant factor in the generation of risks and forms of erosion, as these depend primarily on the intensity of rain [Nunes *et al.* 2011]. In this study, precipitation data used were obtained from the National Agency for Hydraulic Resources (Fr. Agence Nationale des Ressources Hydrauliques – ANRH) based on data from 20 rainfall stations located in the watershed in 1950–1990. We relied on the inverse distance weighting (IDW) interpolation method to extract a precipitation map (Fig. 4) for the Kebir Rhumel Watershed [Nehaï, Guettouche 2020].

Figure 4 shows the distribution of average annual precipitation in the studied rainfall stations of the Kebir Rhumel Basin. Spatial variations of P_a show a growing gradient from the south to the north (Fig. 4). The precipitation is intensive in the north (more 803 mm), medium in the centre (between 412 and 678 mm), and it drops as we move southward (less than 412 mm).

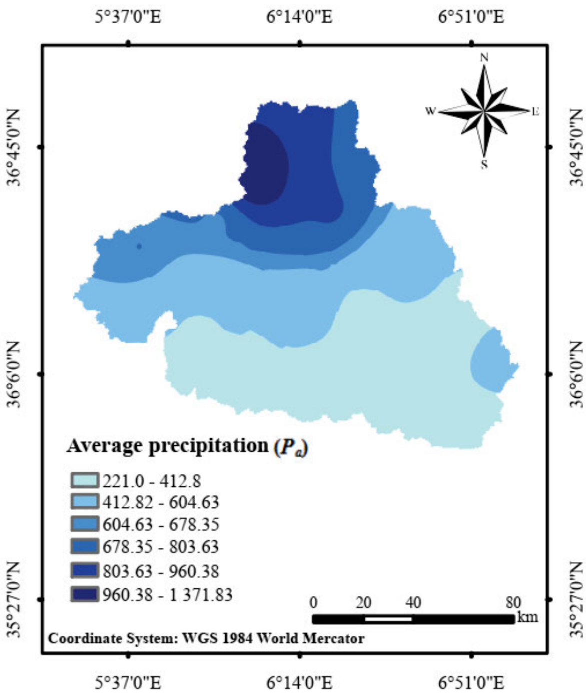

Fig. 4. Map of average annual precipitation (P_a); source: own elaboration

Soil protection coefficient (X_a)

The X_a factor is among decisive factors in the EPM model. It is directly related to the vegetation cover which plays a significant part in reducing erosion. The X_a factor can be based on calculations of the Normalized Difference Vegetation Index (*NDVI*). The surface quality varies depending on seasons and

NDVI values range from −1 to +1, where low values correspond to the absence of vegetation, while high values indicate dense vegetation [Sahli *et al.* 2019]. *NDVI* estimation was carried out based on a multitemporal analysis of Landsat (5 and 8) images. We calculated the annual average for six time periods (1985, 1993, 2001, 2011, 2014 and 2018), shown in Figure 5.

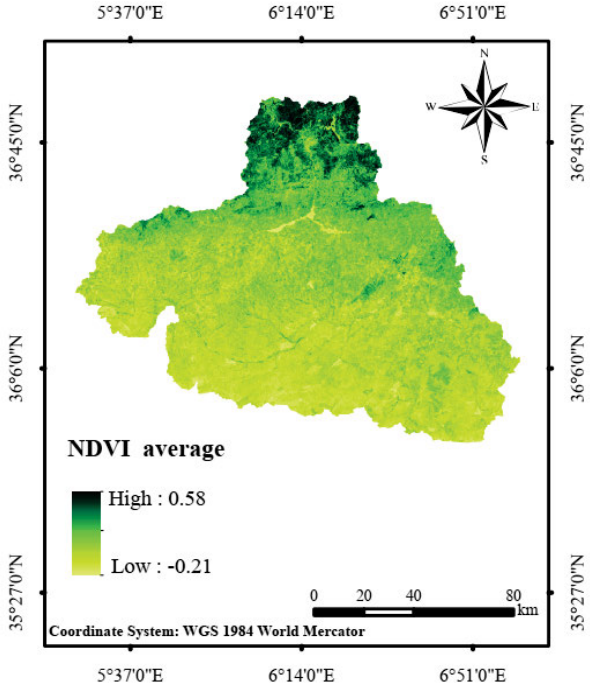

Fig. 5. Map of average Normalized Difference Vegetation Index (*NDVI*); source: own elaboration

The soil protection factor (X_a) is dedicated to the vegetation cover of any type. Vegetation helps to stabilise soil and protect it from erosion, as it slows down the speed of flow and helps to increase water infiltration in the soil. The X_a value ranges from 0.05 for areas with dense vegetation to 1.0 for bare soil [Sakuno *et al.* 2020]. To determine the X_a coefficient, we followed the methodology proposed by Zorn and Komac [2008], where X_a was estimated by the use of a modified *NDVI* (X_a *NDVI*) [Chaaouan *et al.* 2013], using equations shown in Table 3.

The soil protection coefficient (X_a) was estimated according to EPM guide (Tab. 4) [Gavrilovic 1988].

Table 3. Equations for calculating the soil protection factor (X_a)

Data period used for extraction *NDVI*	X_a equation
1985	$X_a = -1.457\ (NDVI - 0.686)$
1993	$X_a = -1.461\ (NDVI - 0.684)$
2001	$X_a = -1.380\ (NDVI - 0.724)$
2011	$X_a = -1.089\ (NDVI - 0.918)$
2014	$X_a = -1.663\ (NDVI - 0.601)$
2018	$X_a = -1.799\ (NDVI - 0.555)$
Average *NDVI*	$X_a = -1.632\ (NDVI - 0.612)$

Explanations: *NDVI* = Normalized Difference Vegetation Index.
Source: own elaboration.

Table 4. Soil protection coefficient values (X_a) acc. to Erosion Potential Method (EPM)

Coefficient of soil cover	X_a factor	Area (%)
Mixed and dense forest and thin forest with a grove	[0.05; 0.20]	0.257
Coniferous forest with little grove, scarce bushes, bushy prairie	(0.20; 0.40]	5.213
Damaged forest and bushes, pasture	(0.40; 0.60]	15.898
Damaged pasture and cultivated land	(0.60; 0.80]	55.271
Areas without vegetal cover	(0.80; 1.00]	23.357

Source: own elaboration.

The following image represents the average soil protection coefficient (X_a) in the study area (Fig. 6).

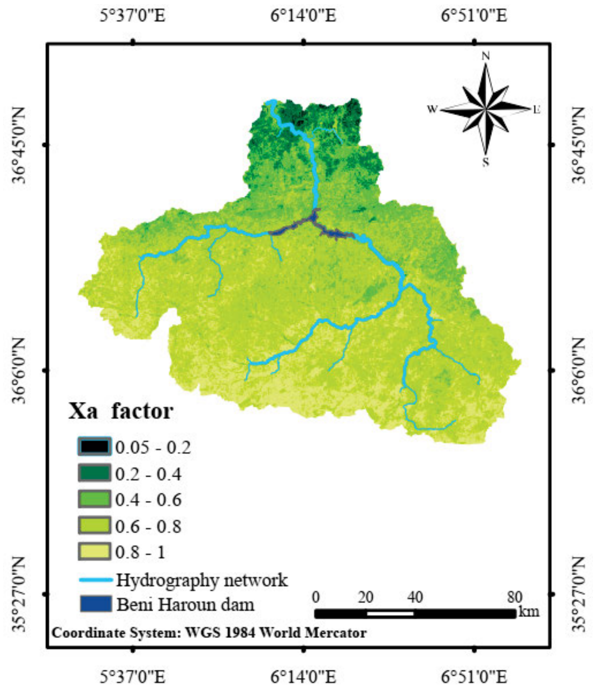

Fig. 6. Map of average soil protection coefficient (X_a); source: own elaboration

The results (Tab. 4) indicate the land cover condition in the Kebir Rhumel Watershed as shown in Figure 6. The category of pastures and cultivated lands (0.6–0.8) represents the most prevalent category in the watershed which accounts for 55.27% of the total area due to the agricultural activity and tillage effects in the region. It is followed by areas without vegetation cover (0.8–1.0) occupying 23.35% of the surface area. The area is covered by rocks and mountain peaks. In the category of damaged forest and bushes, pasture (0.4–0.6), occupies 15.89% of the total area, where overgrazing, deforestation, and forest fires contributed to a lower surface vegetation cover in the Kebir Rhumel Watershed. Finally, forest with little grove, scarce bushes, bushy prairie, mixed and dense forest, and thin forest with a grove (0.05–0.4) cover 5.47% of the total area. This is vivid in the north of the watershed.

Soil erodibility coefficient (*Y*)

Soil erodibility is an important factor in the EPM model. It represents the vulnerability of soil particles to separation and transportation due to water splash and/or surface runoff [Behera *et al.* 2020; Bou-imajjane *et al.* 2020]. In this study, soil data were provided via the Soil Grids map, which is developed and preserved by the ISRIC–World Soil Information, while soil erodibility (*Y*) factor (Fig. 7) was calculated using the model developed by Sharpley and Williams (eds.) [1990] (Eq. 13).

$$Y = \left\{0.2 + 0.3\exp\left[0.0256SAN\left(1 - \frac{SIL}{100}\right)\right]\right\}\left(\frac{SIL}{CLA + SIL}\right)^{0.3}$$
$$\left[1.0 - \frac{0.25\mathrm{C}}{\mathrm{C} + \exp(3.72 - 2.95\mathrm{C})}\right]\left[1.0 - \frac{0.7\mathrm{SN1}}{SN1 + \exp(-5.51 + 2.95SN1)}\right] \quad (13)$$

where *SAN*, *SIL*, *CLA* and C are sand, silt, clay percentages, respectively, and also organic carbon content. *SN*1 is the subtracted sand content of 1 and divided by 100 (Eq. 14).

$$SN1 = 1 - \frac{SAN}{100} \quad (14)$$

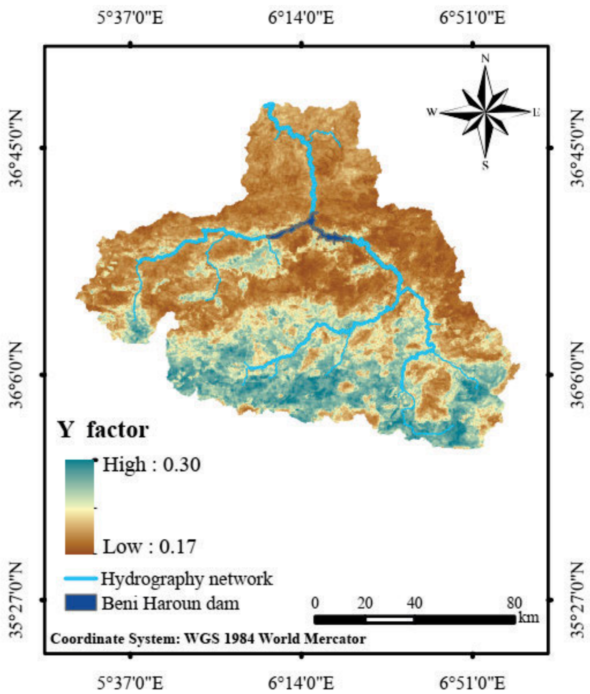

Fig. 7. Map of soil erodibility coefficient; source: own elaboration

Existing erosion indicator (*φ*)

Coefficient *φ* indicates the grade of expressed erosion processes in the watershed, where it specifies the areas affected by erosion (streams, rivers, ravines, alluvial deposits or the entire watershed), with its value ranging between 0.1 and 1.0 (Tab. 5, Fig. 8) [AbdulWahab, Jasim 2019; Gavrilovic 1988]. Data for evaluating the existing erosion indicator (*φ*) were acquired using the methodology proposed by Zorn and Komac [2008], and the calculation of the factor was based on Landsat 5 and 8 satellite images. They contain an "MTL" file which provides information on the images. The *φ* factor is calculated as follows (Eq. 15):

$$\varphi = \sqrt{\frac{TM3}{Q_{\max}}} \text{ and } \varphi = \sqrt{\frac{TM4}{Q_{\max}}} \quad (15)$$

where: *TM*3 = band 3 of Landsat image 5, $Q_{\max}$ = radiance maximum of band 3; *TM*4 = band 4 of Landsat image 8, $Q_{\max}$ = radiance maximum of band 4.

Table 5. Type of soil erosion as a function of existing erosion indicator (*φ*)

Coefficient of type and extent of erosion	*φ*
Little erosion on watershed	<0.20
Erosion in waterways on 20–50% of the catchment area	(0.2; 0.4]
Erosion in rivers, gullies and alluvial deposits, karstic erosion	(0.4; 0.6]
50–80% of catchment area affected by surface erosion and landslides	(0.6; 0.8]
Whole watershed affected by erosion	(0.8; 1.0]

Source: own elaboration.

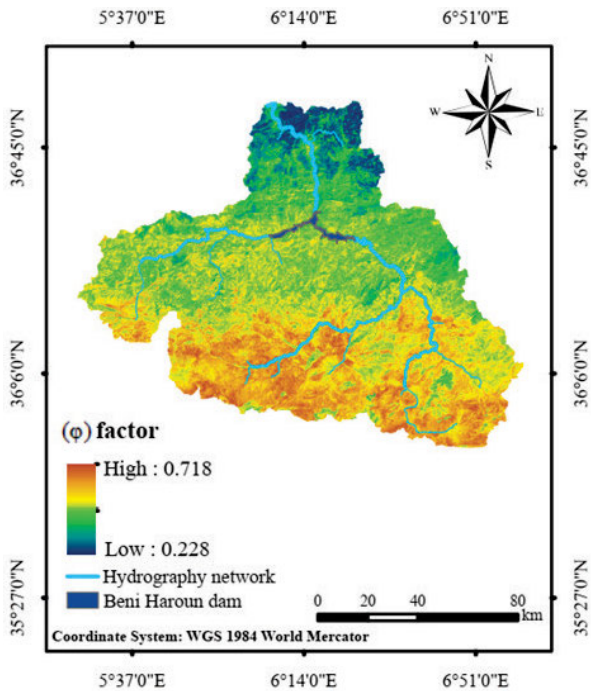

Fig. 8. Map of existing erosion indicator (*φ*); source: own elaboration

The 3rd band in the Landsat 5 satellite image calculated by the following Equation:

$$TM3 = \frac{\pi \cdot L_\lambda \cdot d^2}{Esun_\lambda \cdot \cos\theta_s} \quad (16)$$

$$L_\lambda = \left(\frac{L_{\max\lambda} - L_{\min\lambda}}{Q_{\text{cal max}} - Q_{\text{cal min}}}\right) \cdot (Q_{\text{cal}} - Q_{\text{cal min}}) + L_{\min} \quad (17)$$

The maximum value of the radiance Q_{max} calculated by the following Equation:

$$Q_{\max} = \frac{\pi \cdot (l_{\max} - l_{\min}) + l_{\min} \cdot d^2}{ESUN_\lambda \cdot \cos\theta_s} \tag{18}$$

where: L_λ = spectral radiance at the opening of the sensor ($W \cdot m^{-2} \cdot sr^{-1} \cdot \mu m^{-1}$); Q_{cal} = quantised value of pixel calibrated in Digital Number (DN); $Q_{cal\ min}$ = minimum quantified value of the calibrated pixel corresponds to $L_{min\lambda}$ (DN) = 1; $Q_{cal\ max}$ = maximum quantised value of the calibrated pixel (corresponds to $L_{max\lambda}$), DN = 255; L_{min} = spectral radiance at the sensor which is scaled $Q_{cal\ min}$ ($W \cdot m^{-2} \cdot sr^{-1} \cdot \mu m^{-1}$); L_{max} = spectral radiance at the sensor which is scaled $Q_{cal\ max}$ ($W \cdot m^{-2} \cdot sr^{-1} \cdot \mu m^{-1}$); π = mathematical constant equal to 3.14159; d = distance inter the Earth and Sun (astronomical units); $ESUN_\lambda$ = mean solar exoatmospheric spectral irradiance ($W \cdot m^{-2} \cdot \mu m^{-1}$); θ_s = Sun zenith angle (degrees); θ_s = 90 – sun elevation.

Slope index (J_a, %)

The slope inclination derived from the topography is considered as the major factor in increasing soil sensitivity under the influence of rainfalls. The flow velocity increases with growing slope and this affects an increase in sediment production and transportation to the watershed [Roose 1994]. The coefficient was extracted using the DEM (Digital Elevation Model). Slopes were classified into five categories ranging from (0–10) to 40% [Zahnoun *et al.* 2019], as shown in Figure 9.

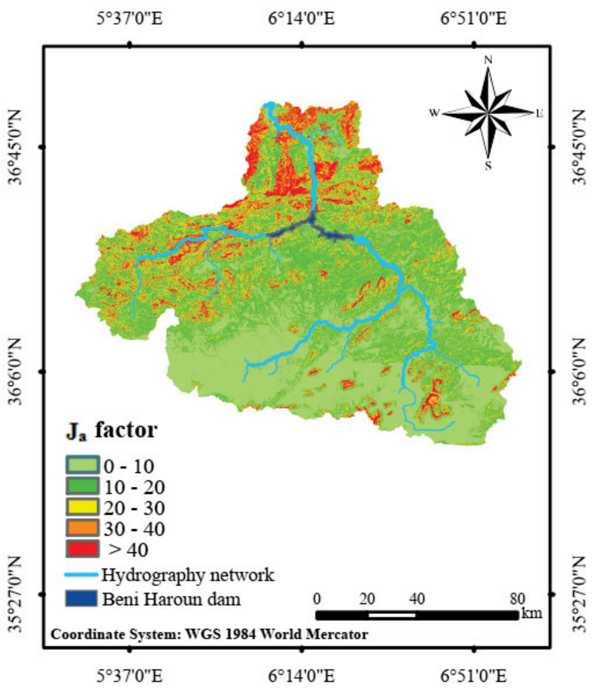

Fig. 9. Map of slope index (J_a); source: own study

The distribution of slope classes (Fig. 9, Tab. 6) shows that those in general very low to moderate (<30%) are dominant. They represent more than 85.45% and occupy 7555.63 km² of the total surface area. High to very high slopes represent 14.55% for classes over 30% and are concentrated in the northern and eastern parts of the watershed.

Table 6. Average slopes coefficient (J_a)

Classes of J_a (%)	Area	
	km²	%
Very low ≤10	3608.33	40.81
Low (10; 20]	2524.52	28.55
Moderate (20; 30]	1422.78	16.09
High (30; 40]	704.95	7.97
Very high >40	582.29	6.58

Source: own elaboration.

To estimate the total amount of eroded sediments ($Mg \cdot km^{-2} \cdot y^{-1}$) and to facilitate comparison between existing results, we extracted the density map (Fig. 10) from the website https://soilgrids.org.

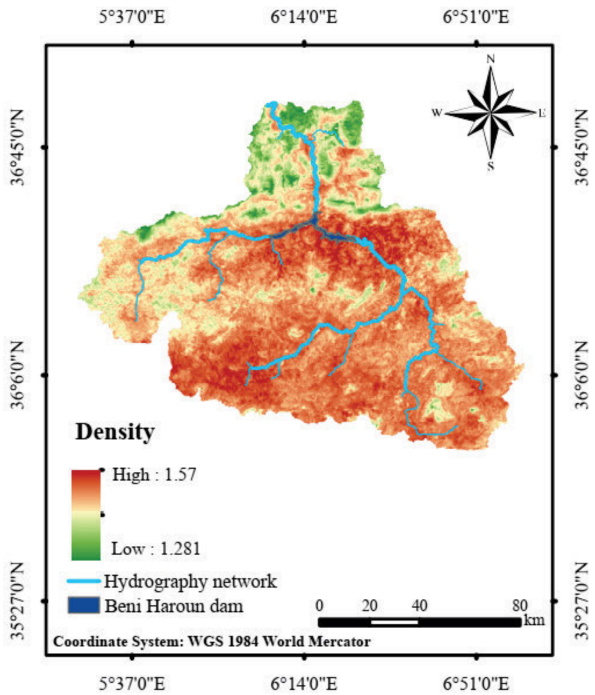

Fig. 10. The density (ρ) map; source: own elaboration

RESULTS AND DISCUSSION

EROSION INTENSITY COEFFICIENT (Z)

The erosion intensity coefficient (Fig. 11) indicates the probability and intensity of erosion, and it has the ability to track the severity of erosion in the watershed. It depends on four factors that control erosion development (soil erodibility, soil protection, topography, and existing erosion indicator) but do not take into account climate capabilities (P_a, T) [Ahmed *et al.* 2019; Efthimiou *et al.* 2016; Kostadinov *et al.* 2008]. It can be calculated through (Eq. 3).

Results obtained (Tab. 7) show that most of the erosion intensity is occupied by the medium erosion class (0.4–0.7) which covers about 4977.54 km² (56.60%) of the total area. It is followed

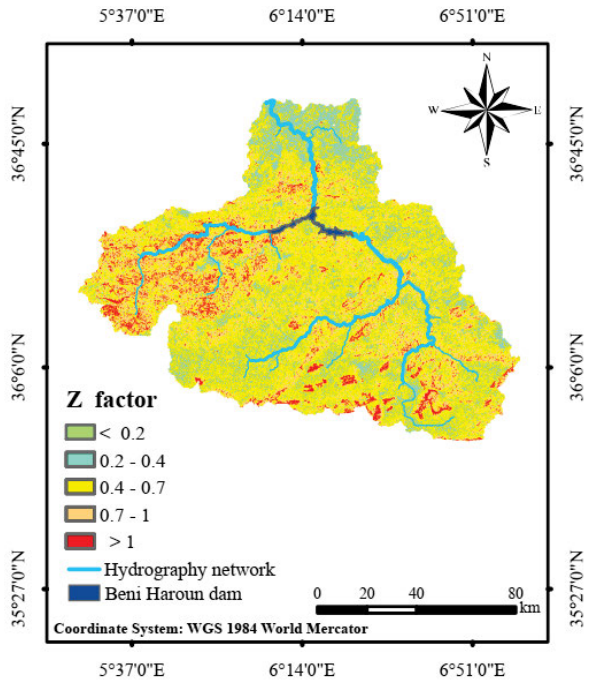

Fig. 11. Map of erosion intensity coefficient (*Z*); source: own study

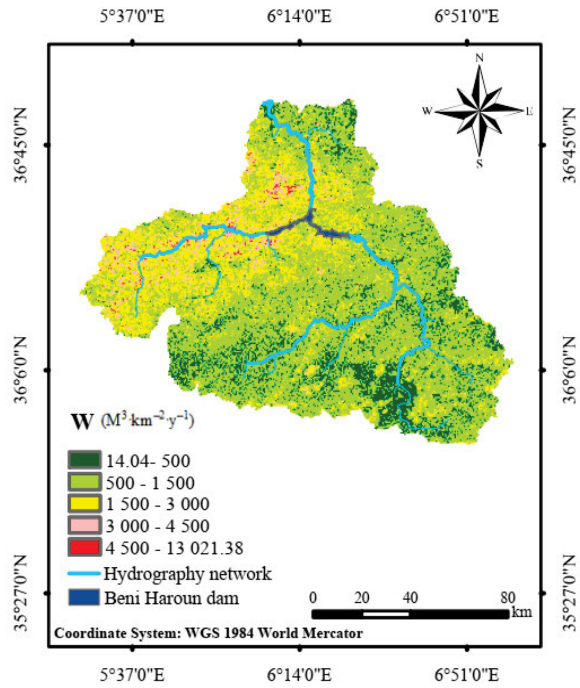

Fig. 12. Map of average annual soil erosion (*W*); source: own study

Table 7. Classification of erosion intensity *Z* coefficient values

Potential erosion coefficient	Classes of (*Z*)	Area	
		(km^2)	(%)
Very slight erosion	≤0.2	98.38	1.11
Slight erosion	(0.2; 0.4]	1 232.80	14.02
Medium erosion	(0.4; 0.7]	4 977.54	56.60
Severe erosion	(0.7; 1.0]	1 961.83	22.31
Excessive erosion	>1.0	523.14	5.94

Source: own study.

by the severe erosion of 1961.83 km^2 (22.31%), then slight erosion (14.02%), excessive erosion (5.94%), and a very slight erosion class (1.11%).

AVERAGE ANNUAL SOIL EROSION (*W*)

After combining parameter *Z* with climatic factors (P_a, T) according to Equation (1), we obtain the average annual volume of detached soil (m^3·km^{-2}·y^{-1}), as shown in Figure 12.

The combination of various factors according to Gavrilović model produced a map of spatial distribution of the soil loss estimation by water erosion (Mg·km^{-2}·y^{-1}) according to Equation (4) (as shown in Fig. 13). To compare the final results obtained, we classified the severity of soil loss into five categories (Tab. 8, Fig. 14).

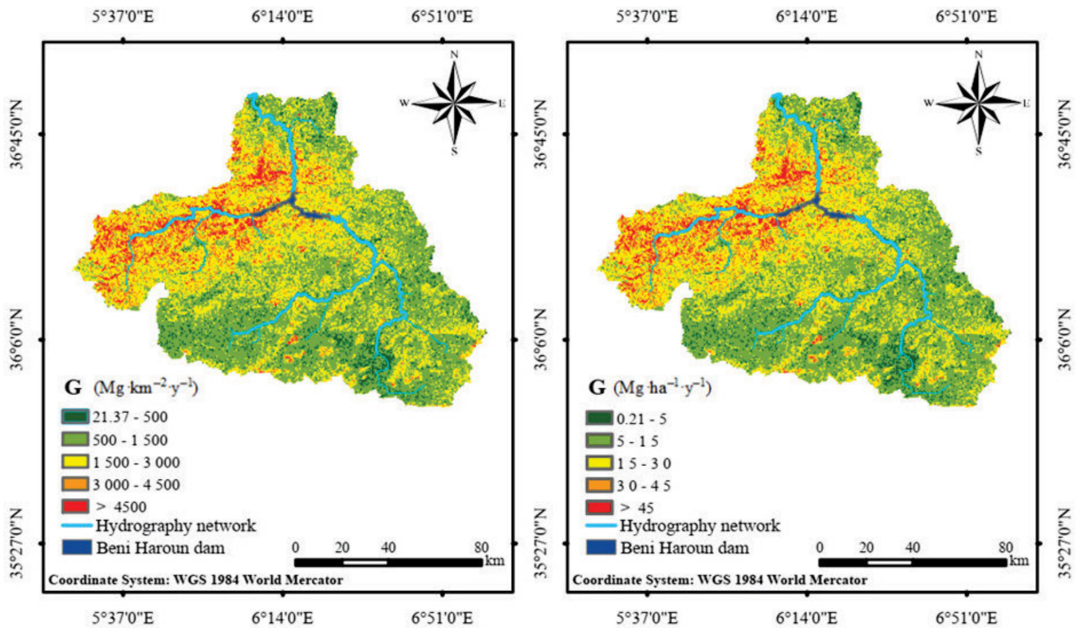

Fig. 13. Map of soil loss (*G*) estimation of Kebir Rhumel watershed; source: own study

Table 8. Annual soil loss in Kebir Rhumel watershed

Annual soil loss	Classes of *G* ($Mg{\cdot}km^{-2}{\cdot}y^{-1}$)	Area	
		(km^2)	(%)
Very low erosion	≤500	435.95	4.93
Low erosion	(500; 1 500]	4 106.68	46.44
Moderate erosion	(1 500; 3 000]	2 996.89	33.89
High erosion	(3 000; 4 500]	922.32	10.43
Very high erosion	>4 500	380.25	4.30

Explanation: *G* = average annual soil erosion.
Source: own estudy.

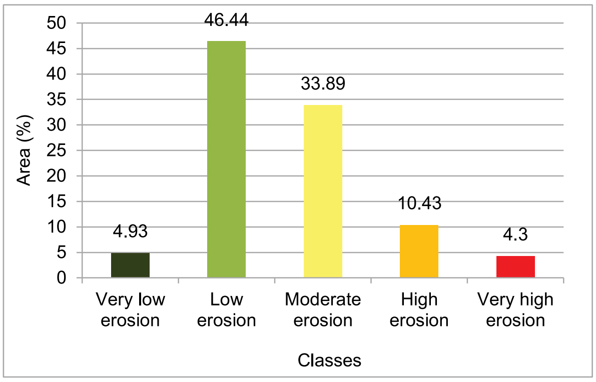

Fig. 14. Area classes of the soil loss of the Kebir Rhumel Watershed; source: own study

Figure 14 represent the area classes of the soil loss in the Kebir Rhumel Watershed.

In the study area, possible soil losses were divided into five categories, i.e. very low, low, moderate, high and very high. This enabled to visualise spatial distribution of erosion (Tab. 8, Fig. 14). The results show an average annual soil loss of 1792 $Mg{\cdot}km^{-2}{\cdot}y^{-1}$ equivalent to 17.92 $Mg{\cdot}ha^{-1}{\cdot}y^{-1}$. Low erosion class (500–1500) covers about 4106.68 km^2 where it covers 46.44% of the total area. It is followed by the moderate erosion class (1500–3000) that covers 33.89% of the total area. These areas correspond to low slopes, damaged pasture, and cultivated land, and it is considered one of the most active agricultural areas in the basin. The high erosion class (10.43%) and very low erosion class (4.93%), is finally followed by a very high erosion class that covers 4.30% of the total area; these areas correspond to steep slopes, rugged mountain terrain, and arid land.

DISCUSSION

The effective sediment volume transported to the catchment outlet is determined by the retention equation (*DR*) (Eq. 7), which provided results shown in Table 9. The *DR* was applied to the average annual soil loss, which resulted in estimates of sediment productivity at the catchment outlet (average yield annual sediment). This estimates the amount of sediment retained along the watershed. The specific sediment yield (*SSY*) was obtained by the total soil loss multiplied by the *DR* (Tab. 9).

Table 9. Specific sediment yield (*SSY*) by Erosion Potential Method and *SSY* from the hydrometric stations in the watershed

Station	Area (km^2)	*G* ($Mg{\cdot}km^{-2}{\cdot}y^{-1}$)	*DR*	*SSY* by EPM model	*SSY* by hydrometric station
				($Mg{\cdot}km^{-2}{\cdot}y^{-1}$)	
El Ancer	8 740.0	1 792.35	0.457	819.10	848.39
Grarem	4 072.7	1 339.46	0.533	713.93	741.12
Dhemcha watershed	3 399.0	2 246.61	0.448	1 006.48	1 030.05

Explanations: *G* = average annual soil erosion, *DR* = retention coefficient.
Source: own study.

The results of this research were compared with other studies conducted in the Kebir Rhumel Watershed to estimate soil erosion by considering different measurements at the hydrometric stations and bathymetric surveys in the Beni Haroun Dam, for example Marouf and Remini [2011] and Tamrabet *et al.* [2019].

According to the study by Marouf and Remini [2011], the annual transport of sediment yield at the El Ancer hydrometric station is 850 $Mg{\cdot}km^{-2}{\cdot}y^{-1}$, while Grarem station recorded an annual sediment yield of 741.12 $Mg{\cdot}km^{-2}{\cdot}y^{-1}$. The study conducted by Tamrabet *et al* [2019] over a period of 30 years in the Dehamecha Watershed recorded an annual sediment yield of 1030.05 $Mg{\cdot}km^{-2}{\cdot}y^{-1}$. The results show that the Dehamecha Watershed is the most vulnerable to soil loss and this can be explained by the presence of mountainous terrain and steep slopes that contributed to an increased flow of sediments to the basin's outlet.

According to the last bathymetric survey conducted by the Marine Studies Laboratory (LEM) from 22 July to 23 September 2013, the annual siltation volume at the Beni Haroun Dam is 8.3 mln m^3, a drained surface area of 7472 km^2 [Toumi, Remini 2018] with an average density of 1.4 $Mg{\cdot}m^{-3}$, so the average erosion is equal to 1555.14 $Mg{\cdot}km^{-2}{\cdot}y^{-1}$. At the level of the Beni Haroun Watershed (7472 km^2), the EPM model estimated the average annual soil loss at 1760.78 $Mg{\cdot}km^{-2}{\cdot}y^{-1}$, where these results were very close to those of the bathymetric survey (2013).

The EPM model gave satisfactory results in estimating the average soil erosion and annual average sediment productivity in the watershed compared to the results recorded in the hydrometric stations. The EPM is one of models efficient in estimating the average soil erosion by water erosion, as many studies conducted using the EPM model in many countries of the world have given satisfactory results [Efthimiou *et al.* 2017; 2016; Lense *et al.* 2020].

CONCLUSIONS

The main objective of our study is to map the distribution of areas susceptible to soil erosion and estimate the average annual soil loss. The Erosion Potential Method (EPM) has been based on available products and data from satellite images using the environment of geographic information systems (GIS). This model involves the integration of several different factors related to climate annual precipitation (P_a), temperature (T), soil protection (X_a), topographic features (slope J_a), erodibility factor (Y), and the degree of erosion (φ).

The implementation of Gavrilović's EPM equation allowed a quantitative estimation of soil losses. This work presents the first erosion risk maps for the Kebir Rhumel Watershed. Results obtained show that average soil losses by water erosion is 17.92 $Mg \cdot ha^{-1} \cdot y^{-1}$, with 80.33% of the total area is exposed to low and moderate risks of erosion.

Terrain alterations along with high J_a factor and rainfall make these areas more susceptible to soil erosion. We can analyse spatial distribution and expected magnitude of soil loss based on areas that are most exposed to the soil loss risk and this helps to implement appropriate protection measures and comprehensive land management practices in the Kebir Rhumel Watershed.

Gavrilović's method is advantageous because it is fast and effective in estimating soil losses due to water erosion. In addition, the EPM can be applied when physical and climatic data are scarce and in areas where soil erosion research has not been previously implemented.

REFERENCES

AbdulWahab F., Jasim S. 2019. Building a model for the risk of water erosion in Kifri Basin by the use of fuzzy logic. Journal of Tikrit University for Humanities. Vol. 26. No. 9 p. 281–257. DOI 10.25130/hum.v26i9.819.

Abu Hammad A. 2011. Watershed erosion risk assessment and management utilizing revised universal soil loss equation-geographic information systems in the Mediterranean environments. Water and Environment Journal. Vol. 25 p. 149–162. DOI 10.1111/j.1747-6593.2009.00202.x.

Ahmed A., Adil D., Hasna B., Elbachir A., Lazaar R. 2019. Using EPM Model and GIS for estimation of soil erosion in Souss Basin, Morocco. Turkish Journal of Agriculture – Food Science and Technology. Vol. 7 p. 1228–1232. DOI 10.24925/turjaf.v7i8.1228-1232.2562.

Behera M., Sena D.R., Mandal U., Kashyap P.S., Dash S.S. 2020. Integrated GIS-based RUSLE approach for quantification of potential soil erosion under future climate change scenarios. Environmental Monitoring and Assessment. Vol. 192, 733 p. 1–18. DOI 10.1007/s10661-020-08688-2.

Bouguerra H., Bouanani A., Khanchoul K., Derdous O., Tachi S.E. 2017. Mapping erosion prone areas in the Bouhamdane watershed (Algeria) using the revised universal soil loss equation through GIS. Journal of Water and Land Development. No. 32 p. 13–23. DOI 10.1515/jwld-2017-0002.

Bouhadeb C.E., Menani M.R., Bouguerra H., Derdous O. 2018. Assessing soil loss using GIS based RUSLE methodology. Case of the Bou Namoussa watershed – North-East of Algeria. Journal of Water and Land Development. No. 36 p. 27–35. DOI 10.2478/jwld-2018-0003.

Bou-imajjane L., Belfoul M.A., Elkadiri R., Stokes M. 2020. Soil erosion assessment in a semi-arid environment: A case study from the Argana Corridor, Morocco. Environmental Earth Sciences. Vol. 79 p. 1–14. DOI 10.1007/s12665-020-09127-8.

Cerdà A., Doerr S.H. 2008. The effect of ash and needle cover on surface runoff and erosion in the immediate post-fire period. Catena. Vol. 74 p. 256–263. DOI 10.1016/j.catena.2008.03.010.

Chaaouan J., Faleh A., Sadiki A., Mesrar H. 2013. Télédétection, sig et modélisation de l'érosion hydrique dans le bassin versant de l'oued Amzaz, Rif Central [Remote sensing, sig and modeling of water erosion in the watershed of Wadi Amzaz, Central Rif]. Revue française de photogrammétrie et de télédétection. No. 203 p. 19–25. DOI 10.52638/rfpt.2013.26.

Dragičević N., Karleuša B., Ožanić N. 2017. Erosion potential method (Gavrilović method) sensitivity analysis. Soil and Water Research. Vol. 12 p. 51–59. DOI 10.17221/27/2016-SWR.

Efthimiou N., Lykoudi E., Karavitis C. 2017. Comparative analysis of sediment yield estimations using different empirical soil erosion models. Hydrological Sciences Journal. Vol. 62 p. 2674–2694. DOI 10.1080/02626667.2017.1404068.

Efthimiou N., Lykoudi E., Panagoulia D., Karavitis C. 2016. Assessment of soil susceptibility to erosion using the EPM and RUSLE models: The case of Venetikos River Catchment. Global NEST Journal. Vol. 18 p. 164–179. DOI 10.30955/gnj.001847.

Fernandez C., Wu J.Q., McCool D.K., Stöckle C.O. 2003. Estimating water erosion and sediment yield with GIS, RUSLE, and SEDD. Journal of Soil and Water Conservation. Vol. 58 p. 128–136.

Gavrilovic Z. 1988. Use of an empirical method (erosion potential method) for calculating sediment production and transportation in unstudied or torrential streams. In: International Conference on River Regime. 18–20.05.1988 Wallingford, England. Oxon UK. Hydraulics Research Limited, Wallingford p. 411–422.

Gitas I.Z., Douros K., Minakou C., Silleos G.N., Karydas C.G. 2009. Multi-temporal soil erosion risk assessment in N. Chalkidiki using a modified USLE raster model. EARSeL eProceedings. Vol. 8 p. 40–52.

Globevnik L., Holjevic D., Petkovsek G., Rubinic J. 2003. Applicability of the Gavrilovic method in erosion calculation using spatial data manipulation techniques. Proceedings of symposium HS01 held during IUGG2003 at Sapporo, July 2003 International Association of Hydrological Sciences Publications. No. 279 p. 224–233.

Haan C.T., Barfield, B.J., Hayes J.C. 1994. Design hydrology and sedimentology for small catchments. Elsevier. ISBN 978-0-12-312340-4 pp. 588.

Ighodaro I.D., Lategan F.S., Yusuf S.F. 2013. The impact of soil erosion on agricultural potential and performance of Sheshegu community farmers in the Eastern Cape of South Africa. Journal of Agricultural Science. Vol. 5. No. 5 p. 140–147. DOI 10.5539/jas.v5n5p140.

Kostadinov S., Dragović N., Zlatić M., Todosijević M. 2008. Erosion control works and the intensity of soil erosion in the upper part of the river Toplica drainage basin. In: IOP Conference Series: Earth and Environmental Science. IOP Publishing. Vol. 4. No. 1, 012040.

Kunta K. 2009. Effects of geographic information quality on soil erosion prediction. ETH Zurich. ISBN 978-3-906467-84-9 pp. 153.

Lense G.H.E., Moreira R.S., Parreiras T.C., Santana D.B., Bolelli T. de M., Mincato R.L. 2020. Water erosion modeling by the Erosion Potential Method and the Revised Universal Soil Loss Equation: A comparative analysis. Revista Ambiente & Água. Vol. 15(4). DOI 10.4136/ambi-agua.2501.

Marouf N., Remini B. 2011. Temporal variability in sediment concentration and hysteresis in the Wadi Kebir Rhumel Basin of Algeria. HKIE Transactions. Vol. 18 p. 13–21. DOI org/10.1080/1023697X.2011.10668219.

Mazour M., Roose E. 2002. Influence de la couverture végétale sur le ruissellement et l'érosion des sols sur parcelles d'érosion dans les bassins versants du Nord-ouest de l'Algérie. En: Techniques traditionnelles de GCES en milieu méditerranéen [Influence of plant cover on runoff and soil erosion on erosion plots in the watersheds of northwestern Algeria. In: Traditional GCES techniques in the Mediterranean environment]. Eds. E. Roose,

M. Sabir, G. De Noni. Bulletin – Réseau Erosion. No. 21 p. 320–330.

Meddi M., Toumi S. 2015. Spatial variability and cartography of maximum annual daily rainfall under different return periods in Northern Algeria. Journal of Mountain Science. Vol. 12 p. 1403–1421. DOI 10.1007/s11629-014-3084-3.

Meghraoui M., Habi M., Morsli B., Regagba M., Seladji A. 2017. Mapping of soil erodibility and assessment of soil losses using the RUSLE model in the Sebaa Chioukh Mountains (northwest of Algeria). Journal of Water and Land Development. No. 34 p. 205–213. DOI 10.1515/jwld-2017-0055.

Mostephaoui T., Merdas S., Sakaa B., Hanafi M.T., Benazzouz M.T. 2013. Cartographie des risques d'érosion hydrique par l'application de l'équation universelle de pertes en sol à l'aide d'un système d'information géographique dans le bassin versant d'El hamel (Boussaâda) Algérie [Mapping of water erosion risks by applying the universal soil loss equation using a Geographical Information System in El Hamel (Boussaâda) watershed]. A Journal algérien des régions arides. No. Special p. 131–147.

Nearing M.A., Jetten V., Baffaut C., Cerdan O., Couturier A., Hernandez M., Le Bissonnais Y., Nichols M.H., Nunes J.P., Renschler C.S. 2005. Modeling response of soil erosion and runoff to changes in precipitation and cover. Catena. Vol. 61 p. 131–154. DOI 10.1016/j.catena.2005.03.007.

Nehaï S.A., Guettouche M.S. 2020. Soil loss estimation using the revised universal soil loss equation and a GIS-based model: A case study of Jijel Wilaya, Algeria. Arabian Journal of Geosciences. Vol. 13, 152. DOI 10.1007/s12517-020-5160-z.

Nunes A.N., De Almeida A.C., Coelho C.O. 2011. Impacts of land use and cover type on runoff and soil erosion in a marginal area of Portugal. Applied Geography. Vol. 31. No. 2 p. 687–699. DOI 10.1016/j.apgeog.2010.12.006.

Panagos P., Standardi G., Borrelli P., Lugato E., Montanarella L., Bosello F. 2018. Cost of agricultural productivity loss due to soil erosion in the European Union: From direct cost evaluation approaches to the use of macroeconomic models. Land Degradation & Development. Vol. 29 p. 471–484. DOI 10.1002/ldr.2879.

Roose E. 1994. Introduction à la gestion conservatoire de l'eau, de la biomasse et de la fertilité des sols (GCES) [Introduction to the conservation management of water, biomass and soil fertility (GCES)]. Bulletin pédologique de la FAO. No. 70. ISBN 92-5-203451-X pp. 420.

Rousel J.W., Haas R.H., Schell J.A., Deering D.W. 1973. Monitoring vegetation systems in the great plains with ERTS. In: Proceedings of the Third Earth Resources Technology Satellite – 1 Symposium; NASA SP-351 p. 309–317.

Sahli Y., Mokhtari E., Merzouk B., Laignel B., Vial C., Madani K. 2019. Mapping surface water erosion potential in the Soummam watershed in Northeast Algeria with RUSLE model. Journal of Mountain Science. Vol. 16 p. 1606–1615. DOI 10.1007/s11629-018-5325-3.

Sakuno N.R.R., Guiçardi A.C.F., Spalevic V., Avanzi J.C., Silva M.L.N., Mincato R.L. 2020. Adaptation and application of the erosion potential method for tropical soils. Revista Ciência Agronômica. Vol. 51 p. 1–10.

Sekertekin A., Bonafoni S. 2020. Land surface temperature retrieval from Landsat 5, 7, and 8 over rural areas: assessment of different retrieval algorithms and emissivity models and toolbox implementation. Remote Sensing. Vol. 12 p. 294. DOI 10.3390/rs12020294.

Sharda V.N., Mandai D., Ojasvi P.R. 2013. Identification of soil erosion risk areas for conservation planning in different states of India. Journal of Environmental Biology. Vol. 34 p. 219–226.

Sharpley A.N., Williams J.R. (eds.) 1990. EPIC-Erosion/Productivity Impact Calculator. I: Model documentation. II: User manual. USDA. Technical Bulletin. No. 1768 pp. 127.

Solaimani K., Modallaldoust S., Lotfi S. 2009. Investigation of land use changes on soil erosion process using geographical information system. International Journal of Environmental Science & Technology. Vol. 6 p. 415–424. DOI 10.1007/BF03326080.

Tamrabet Z., Marouf N., Remini B. 2019. Quantification of suspended solid transport in Endja watercourse [Dehamecha basin-Algeria]. GeoScience Engineering. No. 4 p. 71–91. DOI 10.35180/gse-2019-0025.

Tang Q., Xu Y., Bennett S.J., Li Y. 2015. Assessment of soil erosion using RUSLE and GIS: A case study of the Yangou watershed in the Loess Plateau, China. Environmental Earth Sciences. Vol. 73 p. 1715–1724. DOI 10.1007/s12665-014-3523-z.

Toumi A., Remini B. 2018. Perte de la capacité de stockage d'eau au barrage de Beni Haroun, Algérie [Loss of water storage capacity at the Beni Haroun dam, Algeria]. Systèmes Agraires et Environnement. Vol. 2 p. 80–97.

Zahnoun A.A., Makhchane M., Chakir M., Al Karkouri J., Watfae A. 2019. Estimation and cartography the water erosion by integration of the Gavrilovic "EPM" model using a GIS in the Mediterranean watershed: Lower Oued Kert watershed (Eastern Rif, Morocco). International Journal of Advance Research, Ideas and Innovations in Technology. Vol. 5 p. 367–374.

Zakerinejad R., Maerker M. 2015. An integrated assessment of soil erosion dynamics with special emphasis on gully erosion in the Mazayjan basin, southwestern Iran. Natural Hazards. Vol. 79 p. 25–50. DOI 10.1007/s11069-015-1700-3.

Zanter K. 2019. Landsat 8 (L8) data users handbook. Version 5.0. Sioux Falls, SD. EROS pp. 106.

Zemljic M. 1971. Calcul du debit solide – Evaluation de la vegetation comme un des facteurs antierosif [Calculation of the solid flow – Evaluation of the vegetation as one of the anti-erosive factors]. In: International Symposium Interpraevent. Villaco. Vol. 2 p. 379–391.

Zorn M., Komac B. 2008. The response of soil erosion to land-use change with particular reference to the last 200 year (Julian Alps, Western Slovenia). [24th Conference of the Danubian Countries on the Hydrological Forecasting and Hydrological Bases of Water Management]. [02–06.2008 Bled, Slovenia].